Draft version October 21, 2025
Typeset using LaTeX **twocolumn** style in AASTeX631

Radiation pressure and equation of state are important in the envelope unbinding process in common envelope evolution

Zhuo Chen (陈卓)[1]

[1] *Institute for Advanced Study, Tsinghua University*
Beijing 100084, China

Submitted to ApJL

ABSTRACT

In common envelope evolution, the ultimate unbinding of the envelope during the plunge-in phase involves complex and poorly understood physical processes that may give rise to luminous red novae. In this work, we investigate the roles of radiation and gas pressures in envelope unbinding. We perform a parameter space survey using a one-dimensional radiation hydrodynamic model that is solved by `Guangqi` to study the impact of key parameters on the mass unbound fraction and resulting light curves. The parameters include the radiation to gas energy ratio $\mathcal{E}/e_{\rm g} \in [0.2, 3.2]$, speed of the ejecta, ranging from 70% to 85% of the escape velocity, and equation of state (EoS). For comparison, we also perform simulations with pure hydrodynamic or no radiation pressure effect conditions. Our simulations demonstrate that the radiation pressure is crucial for the envelope unbinding. Specifically, the radiation pressure may dominate in a high opacity and high luminosity layer just below the recombination front, where it can accelerate the sub-escape material to escape velocities. A realistic EoS further enhances the pressure gradient, especially during the early phase of ejection at small radii, promoting additional envelope ejection. Both $\mathcal{E}/e_{\rm g}$ and EoS significantly alter light curve shapes, and provide observable diagnostics for these processes. We show that the relative energy error of all the simulations is no more than 1.4%, and all the simulations are close to convergence.

Keywords: Hydrodynamical simulations (767) — Common envelope evolution(2154)

1. INTRODUCTION

Common envelope evolution (CEE) is one of the most poorly understood stages in binary evolution (Ivanova et al. 2013), owing to the rarity of these events, the challenges of direct observation (Tylenda et al. 2011; Blagorodnova et al. 2017; Cai et al. 2019; Pastorello et al. 2019; Blagorodnova et al. 2021; Pastorello et al. 2021a,b), and its inherent multi-physics complexity. During this phase, the orbital energy of the binary cores is converted into kinetic, thermal, magnetic, and radiation energy. If the orbital energy is deposited in a highly optically thick environment in a short time, such as during the plunge-in phase, the radiation energy/pressure may exceed the gas energy/pressure, which may promote the ejection of the common envelope. After the CEE, the separation between the stellar cores can decrease by up to two orders of magnitude. Depending on the progenitor system, the resulting binaries may subsequently evolve into gravitational wave sources (Dominik et al. 2012), X-ray binaries (Kalogera & Webbink 1998; Xing et al. 2025), or progenitors of type Ia supernovae (Liu et al. 2023). Unfortunately, the gap in our understanding between the CEE phase and its final products remains so large that we cannot yet establish a one-to-one correspondence between binary progenitors and the resulting evolved binaries (Han et al. 2020; Chen et al. 2024).

Numerous three-dimensional (3D) hydrodynamic (Ricker & Taam 2012; Nandez et al. 2014, 2015; Ivanova & Nandez 2016; Nandez & Ivanova 2016; Ohlmann et al.

Corresponding author: Zhuo Chen
chenzhuo_astro@mail.tsinghua.edu.cn

2016; Chamandy et al. 2018; Iaconi et al. 2019; Prust & Chang 2019; Sand et al. 2020; Moreno et al. 2022; Lau et al. 2022a,b; Chamandy et al. 2024) and magnetohydrodynamic (MHD) (Ondratschek et al. 2022; Vetter et al. 2024, 2025) simulations have been carried out to study the final separation problem together with the envelope unbinding problem. Typically, these simulations are performed under the adiabatic assumption, as full modeling the convection and radiation transport in 3D is computationally prohibitive (but see Goldberg et al. (2022) and Lau et al. (2025)). In such adiabatic models, envelope unbinding is primarily ascribed to the pressure gradients and angular momentum transport via turbulence or magnetic fields. However, neglecting radiation transport is a significant simplification. While the adiabatic assumption may be appropriate for a small, low-luminosity envelope early in the interaction, it inevitably breaks down as the envelope expands and becomes more luminous. The recent progress made by Lau et al. (2025) shows that the radiation transport inhibits the ejection of the envelope, compared to the adiabatic simulation, because radiation transport is an effective way to dissipate energy in the optically thin region. On the other hand, radiation pressure is crucial in other areas of stellar evolution, where it is known to efficiently drive powerful stellar winds in objects like Wolf-Rayet (Gräfener et al. 2017; Sander & Vink 2020) and AGB stars (Höfner & Olofsson 2018; Decin 2021). Finally, including radiation transport is essential for predicting the observational signatures of these events (Hatfull et al. 2021; Hatfull & Ivanova 2025) and bridging the gap between theory and observation (Chen & Ivanova 2024).

Alternatively, one-dimensional (1D) models have been developed to better resolve the microphysics of CEE, focusing on recombination energy, convection, and radiation transport. Studies suggest that recombination energy may only play a limited role in envelope unbinding (Grichener et al. 2018; Soker et al. 2018). The role of convection, however, appears more critical. A convective envelope can efficiently transport energy outward, allowing the secondary star to spiral inward (Wilson & Nordhaus 2020, 2022). This inspiral may be halted if the companion encounters a deep, stable radiative layer, a process that could ultimately determine the final binary separation (Hirai & Mandel 2022). Detailed 1D simulations, such as the study of a neutron star and a supergiant system by Fragos et al. (2019), provide the framework for exploring these intricate processes. A key remaining uncertainty in the overall physical process is the role of radiation transport. When the luminosity and opacity are high, radiation pressure can become a dominant force capable of driving an outflow. For instance, simulations modeling the luminous transient AT2019zhd found that the outward radiation pressure may balance gravity (Chen & Ivanova 2024). However, this model did not consider the work done by the radiation pressure on radiation energy, $\mathcal{P}_r : \nabla \mathbf{v}$, (to be explained later), making it only applicable to low radiation pressure cases. Thus, a more self-consistent model with a parameter space survey is needed.

In this work, we conduct a parameter space study of a 1D radiation hydrodynamic (RHD) ejecta model. We systematically examine key parameters, including the ratio of radiation energy to gas energy $\mathcal{E}/e_{\rm g}$, equation of state (EoS), and ejecta velocity, to examine their influence on the fraction of unbound material, the significance of radiation pressure across different regimes, and their observable imprints on the resulting light curves. The paper is organized as follows. Section 2 details our physical framework, including the governing RHD equations, initial and boundary conditions, and ejecta models. Section 3 presents and analyzes our simulation results. Finally, we summarize our conclusions and suggest future research directions in Section 4.

2. PHYSICAL MODEL

2.1. *The governing equations*

We solve the RHD equations in the laboratory frame with flux-limited diffusion (FLD) approximation and a mixture of hydrogen and helium gas species with `Guangqi` (Chen & Bai submitted). Due to the presence of tensor product, for compactness and generality, we write down the governing equations in the vector form, but they are solved in spherical coordinates with spherical symmetry:

$$\frac{\partial \rho}{\partial t} + \nabla \cdot (\rho \mathbf{v}) = 0, \tag{1}$$

$$\frac{\partial \rho \mathbf{v}}{\partial t} + \nabla \cdot (\rho \mathbf{v}\mathbf{v} + p\mathbb{I}) = \rho(\mathbf{a}_{\rm rad} - \nabla\phi), \tag{2}$$

$$\frac{\partial E}{\partial t} + \nabla \cdot [(E+p)\mathbf{v}] = \rho\mathbf{v} \cdot (\mathbf{a}_{\rm rad} - \nabla\phi) + G^0, \tag{3}$$

$$\frac{\partial \mathcal{E}}{\partial t} + \nabla \cdot (\mathbf{F}_r + \mathcal{E}\mathbf{v}) = -G^0 - \mathcal{P}_r : \nabla \mathbf{v}, \tag{4}$$

$$E = \rho\frac{|\mathbf{v}|^2}{2} + e_{\rm g}(\rho, T_{\rm g}), \tag{5}$$

$$G^0 = \kappa_{\rm P}\rho c(\mathcal{E} - a_{\rm r}T_{\rm g}^4) \tag{6}$$

where $\rho, \mathbf{v} = [v_r, 0, 0], p, T_{\rm g}, e_{\rm g}$, and E are the density, radial velocity, pressure, temperature, internal energy, and total energy of the gas, respectively. The radiation and gravitational force accelerations are denoted by $\mathbf{a}_{\rm rad}$ (defined later) and $-\nabla\phi = [-g, 0, 0]$, where $\phi = -GM_\star/r$ is the gravitational potential, and $M_\star$ and G are the mass of the central object and gravitational constant.

The gas and radiation exchange heat at the rate of G^0, in which $\kappa_{\rm P}$ is the Planck mean opacity in the co-moving frame.

We adopt the FLD radiation transport model (Levermore & Pomraning 1981; Levermore 1984), which provides the closure relations between the radiation energy density $\mathcal{E}$, radiation flux $\mathbf{F}_r$, and radiation pressure tensor $\mathcal{P}_r$,

$$\mathbf{F}_r = -\frac{c\lambda(\mathcal{R})}{\kappa_{\rm R}\rho}\nabla\mathcal{E}, \tag{7}$$

$$\mathcal{P}_r = \frac{\mathcal{E}}{2}[(1-f)\mathbb{I} + (3f-1)\mathbf{nn}], \tag{8}$$

where $\kappa_{\rm R}$, c, $\mathbf{n} = \mathbf{F}_r/|\mathbf{F}_r|$ are the Rosseland mean opacity in the co-moving frame, speed of light, and the unit vector in the direction of $\mathbf{F}_r$. The aforementioned radiation acceleration term is calculated by $\mathbf{a}_{\rm rad} = \kappa_{\rm R}\mathbf{F}_r/c = [a_{\rm rad}, 0, 0]$. With dimensional analysis (Colombo et al. 2019), it can be shown that,

$$-\nabla\cdot\mathcal{P}_r \approx \frac{\rho\kappa_{\rm R}\mathbf{F}_r}{c} = \rho\mathbf{a}_{\rm rad}, \tag{9}$$

when $v_{\rm gas}/c \ll 1$ and $\mathbf{F}_r$ is not varying rapidly. Thus, we can equivalently say that the gas is accelerated by the radiation pressure. This approximation is useful in examining the energy conservation of our simulations (Appendix A). Meanwhile, the flux limiter λ and other two dimensionless variables $\mathcal{R}$ and f are calculated by,

$$\lambda(\mathcal{R}) = \frac{2+\mathcal{R}}{6+3\mathcal{R}+\mathcal{R}^2}, \tag{10}$$

$$\mathcal{R} = \frac{|\nabla\mathcal{E}|}{\kappa_{\rm R}\rho\mathcal{E}}, \tag{11}$$

$$f = \lambda + \lambda^2\mathcal{R}^2. \tag{12}$$

These variables make $\mathbf{F}_r$ and $\mathcal{P}_r$ have the following desired asymptotic behaviors with smooth transitions in between,

$$\mathbf{F}_r \rightarrow \begin{cases} c\nabla\mathcal{E}/(3\kappa_{\rm R}\rho) & \text{optically thick,} \\ c\mathcal{E}\mathbf{n} & \text{optically thin,} \end{cases} \tag{13}$$

and

$$\mathcal{P}_r \rightarrow \begin{cases} \mathcal{E}\mathbb{I}/3 & \text{optically thick,} \\ \mathcal{E}\mathbf{nn} & \text{optically thin.} \end{cases} \tag{14}$$

We adopt the same opacity tables from Chen & Ivanova (2024), which combine dust (Semenov et al. 2003) and gas opacities (Malygin et al. 2014). Equation 5 describes the total energy, which includes the recombination energies by incorporating the internal energy through a general EoS $e_{\rm g}(\rho, T_{\rm g})$ consisting of H_2, H, H^+, He, He^+, He^{2+}, and e^- (see Appendix A of Chen & Ivanova (2024)).

In `Guangqi`, the hydrodynamic equations 1-3 (without G^0) are solved by a general EoS HLLC Riemann solver (Chen et al. 2019) with MUSCL scheme and operator unsplit method (Chen & Bai submitted). We set the CFL number to be 0.4.

The radiation and gas energy are coupled in thermodynamics, described by the following thermodynamic and radiation transport equations,

$$\frac{\partial e_{\rm g}}{\partial t} = G^0, \tag{15}$$

$$\frac{\partial\mathcal{E}}{\partial t} + \nabla\cdot[(\mathbf{F}_r + \mathcal{E}\mathbf{v})] + \mathcal{P}_r : \nabla\mathbf{v} = -G^0. \tag{16}$$

Equation 15 and 16 are integrated implicitly by the GMRES Krylov iterative solver with `Petsc` (Balay et al. 1997, 2024). We adopts a relative tolerance of error $\epsilon_r = 10^{-10}$. The thermodynamic system usually has a shorter characteristic timescale than the hydrodynamic system. Thus, to accurately integrate the thermodynamic system after each integration of the hydrodynamic system, we divide the hydrodynamic timestep into $n_{\rm sub} = 6$ substeps, with each sub-timestep increases by a ratio of $q_t = 1.4$, i.e., $\delta t_{m+1} = q_t\delta t_m$, where m is the substep number. We confirm that the choice of parameters enables converged solutions (Appendix B).

2.2. *Computational domain and numerical setups*

Motivated by many CEE simulations with massive binary stars (Fragos et al. 2019; Vetter et al. 2024; Lau et al. 2025), we set the computational domain to be $[r_{\rm in}, r_{\rm out}]$ where $r_{\rm in} = 450R_\odot$, $r_{\rm out} = 1.5\times10^4R_\odot$, and $\odot$ denotes the solar unit. We assume there is a gravitational source with a fixed mass $M_\star = 15M_\odot$ at the origin, representing the binary and common envelope. The cores of the binary system are assumed to orbit at a radius smaller than $r_{\rm in}$, depositing energy into the envelope, providing the envelope some out of equilibrium velocity and energy. Adopting another set of parameters of $M_\star$ and $r_{\rm in}$ can alter individual results quantitatively, but will likely not change the correlations and conclusions that will be drawn from our simulations. The computational domain has a base resolution of $N_x = 1536$, and there is 1 level of mesh refinement that covers $[r_{\rm in}, 2r_{\rm in}]$. The coordinate is stretched such that the cell size increases geometrically, i.e., $\Delta r_{i+1} = 1.0028\Delta r_i$, where i is the index of the cell.

The initial conditions in the computational domain are, $\rho = \rho_0(r_{\rm in}/r)^{1.5}$, $\rho_0 = 10^{-17}{\rm g}\cdot{\rm cm}^{-3}$, $v_r = 0$, and $T_{\rm g} = 200K$. The initial mass and energy in the computational domain are negligible compared to the mass and energy in the ejecta, thus imposing little impact on the dynamics and evolution of the ejecta.

2.3. *Boundary conditions*

The outer boundary is assumed to be optically thin,

$$\frac{\partial(\mathcal{E}r^2)}{\partial r} = 0. \tag{17}$$

To ensure that the outer boundary is optically thin, we set $(\rho\kappa_{\rm R})_{N_x+\frac{1}{2}} = \min\{(\rho\kappa_{\rm R})_{N_x}, 1/(3r_{\rm out})\}$. Here, the subscripts $N_x + \frac{1}{2}$ and N_x denote values at the out boundary and the cell adjacent to it. This operation guarantees that the mean free path of radiation at the outer boundary is at least 3 times of the computational domain length scale. Thus, $\mathcal{P}_r \approx \mathcal{E}\hat{r}\hat{r}$ at the outer boundary, where $\hat{r}$ is the unit radial vector. For the gas, the outer boundary is treated as outflow-only. Specifically, the ghost cell copies the hydrodynamic variables from the outermost computational cell, and we impose $v_r = \max\{v_r, 0\}$ for the ghost cell.

The common envelope (CE) ejecta enters the computational domain through the inner boundary. During the initial ejecta launching phase, we set the inner boundary conditions for radiation and hydrodynamics to match the ejecta's physical properties, including: $\rho, \mathbf{v}, \mathcal{E}$, and $T_{\rm g}$. After the ejection phase, we switch to an inflow-only boundary condition. For this, the ghost cell copies all radiation and hydrodynamic variables from the innermost computational cell, and we impose $v_r = \min\{v_r, 0\}$. Throughout the simulations, we maintain $\partial\mathcal{E}/\partial r = 0$ at the inner boundary, thus, $\mathbf{F}_r = 0$ at the inner boundary. We also find that the inner boundary is always in an optically thick state, thus, $\mathcal{P}_r \approx \mathcal{E}\mathbb{I}/3$ at the inner boundary. While this inner boundary condition is ideal for studying the dynamics of the isolated ejecta with minimal influence from the inner boundary, it is not physically realistic, an issue we discuss further in Section 4.

2.4. *The ejecta models*

We study the dynamics and evolution of time-independent ejecta with a survey of the parameter space. Here, we will sometimes use "ejecta" and "envelope" exchangeably because we study the acceleration of gas to escape velocity, and there are intermediate states. For simplicity, we assume the ejecta in all the models have a fixed mass loss rate of $\dot{M} = 5M_\odot \cdot {\rm yr}^{-1}$ and a fixed duration of $\Delta t = 50$ days, equivalent to $\Delta M_{\rm ej} = 0.685M_\odot$ in mass loss.

In this work, we aim to focus on the dynamics within an isolated ejecta, instead of the whole CE ejecta launching phase, thus $\Delta M_{\rm ej} \ll M_\star$. We extensively explore the impact of the radiation energy ratio $\mathcal{E}/e_{\rm g}$, ratio of the ejecta's speed to the escape speed $\bar{v}_{\rm ej} = v_{\rm ej}/\sqrt{2GM_\star/r_{\rm in}}$, EoS, and radiation pressure on the ability to accelerate the ejecta to escape velocity, as well as their potential impact on the light curves. We classify the models into five groups, distinguished by their microphysics, to address the importance of radiation pressure and EoS. The ejecta speed $\bar{v}_{\rm ej} \in \{0.7, 0.75, 0.8, 0.85\}$ varies within the sub-escape regime, but is still supersonic, to avoid the possible complication of the transonic region. Thus, $\rho_{\rm ej}$ is determined by the fixed $\bar{v}_{\rm ej}$, $r_{\rm in}$ and $\dot{M}$. Meanwhile, we adopt a fixed set of ejecta temperature for each group, such that the baseline group (explained later) has $\mathcal{E}/e_{\rm g} \in \{0.2, 0.4, 0.8, 1.6, 3.2\}$. Overall, the ejecta of all the groups vary from a gas energy dominated state to a radiation energy dominated state, sometimes with a different set of $\mathcal{E}/e_{\rm g}$ due to the differences in EoS, to account for the cases from a small to significant amount of energy release during the plunge-in phase. The five groups of simulations are:

1. Group 1, the baseline group, uses a realistic EoS with hydrogen mass ratio $X = 0.74$ and helium mass ratio $Y = 0.26$, and has $\mathcal{E}$, $\mathbf{F}_r$, and $\mathcal{P}_r$. All other groups have one piece of physics different from group 1, while keeping the density and temperature the same as group 1. Table 1 presents the relevant physical parameters (some explained later) of the models in Group 1.

2. Group 2, a γ-law gas EoS and RHD group, with $\gamma_1 = 1.4$ and mean atomic weight $\mu = 1$. The ejecta models in this group always have lower total energy than group 1, which is measured by ζ_3 (explained later), listed in the 11th column in Table 1.

3. Group 3, a γ-law gas EoS and RHD group, with $\gamma_2 = 1.1$ and mean atomic weight $\mu = 1$. The ejecta models in this group always have higher total energy than group 1, with ζ_3 listed in the 12th column in Table 1.

4. Group 4, the pure hydrodynamic group, uses the same realistic EoS as group 1. The radiation energy $\mathcal{E}$, radiation flux $\mathbf{F}_r$, and radiation pressure $\mathcal{P}_r$ are all set to 0 in this group of simulations. The ζ_3 of this group is listed in the 13th column in Table 1.

5. Group 5, the no radiation pressure effect group. We remove the effect of radiation pressure by setting $\mathbf{a}_{\rm rad} = 0$ (because of Equation 9) and $\mathcal{P}_r : \nabla\mathbf{v} = 0$. We still consider the radiation and gas energy coupling, and the radiation energy

model	Group1 (G1)									G2	G3	G4	G5
Ejecta	$\mathcal{E}/e_{\rm g}$	$\bar{v}_{\rm ej}$	$\rho_{\rm ej}$ ($\rm g{\cdot}cm^{-3}$)	$T_{\rm g}$ (K)	$\dot{\mathcal{E}}$ ($\rm erg{\cdot}s^{-1}$)	$p_{\rm rad}/p$	ζ_1	ζ_2	$\zeta_{3,G1}$	$\zeta_{3,G2}$	$\zeta_{3,G3}$	$\zeta_{3,G4}$	$\zeta_{3,G5}$
(1)	(2)	(3)	(4)	(5)	(6)	(7)	(8)	(9)	(10)	(11)	(12)	(13)	(14)
E1	0.20	0.70	3.24×10^{-9}	3.76×10^{4}	1.47×10^{39}	0.300	0.490	0.855	0.928	0.685	1.050	0.855	0.928
E2	0.20	0.75	3.03×10^{-9}	3.68×10^{4}	1.44×10^{39}	0.303	0.563	0.922	0.994	0.754	1.112	0.922	0.994
E3	0.20	0.80	2.84×10^{-9}	3.60×10^{4}	1.42×10^{39}	0.305	0.640	0.994	1.064	0.828	1.178	0.994	1.064
E4	0.20	0.85	2.67×10^{-9}	3.54×10^{4}	1.40×10^{39}	0.306	0.723	1.070	1.140	0.907	1.251	1.070	1.140
E5	0.40	0.70	3.24×10^{-9}	4.58×10^{4}	3.23×10^{39}	0.540	0.490	0.893	1.054	0.800	1.245	0.893	1.054
E6	0.40	0.75	3.03×10^{-9}	4.49×10^{4}	3.20×10^{39}	0.546	0.563	0.963	1.123	0.868	1.306	0.963	1.123
E7	0.40	0.80	2.84×10^{-9}	4.41×10^{4}	3.20×10^{39}	0.552	0.640	1.037	1.196	0.942	1.372	1.037	1.196
E8	0.40	0.85	2.67×10^{-9}	4.34×10^{4}	3.17×10^{39}	0.558	0.723	1.117	1.275	1.021	1.444	1.117	1.275
E9	0.80	0.70	3.24×10^{-9}	5.55×10^{4}	6.98×10^{39}	0.962	0.490	0.926	1.274	1.018	1.559	0.926	1.274
E10	0.80	0.75	3.03×10^{-9}	5.45×10^{4}	6.93×10^{39}	0.973	0.563	0.995	1.340	1.085	1.615	0.995	1.340
E11	0.80	0.80	2.84×10^{-9}	5.35×10^{4}	6.89×10^{39}	0.983	0.640	1.069	1.412	1.157	1.677	1.069	1.412
E12	0.80	0.85	2.67×10^{-9}	5.26×10^{4}	6.84×10^{39}	0.993	0.723	1.148	1.489	1.234	1.746	1.148	1.489
E13	1.60	0.70	3.24×10^{-9}	6.75×10^{4}	1.53×10^{40}	1.725	0.490	0.965	1.724	1.468	2.124	0.965	1.724
E14	1.60	0.75	3.03×10^{-9}	6.62×10^{4}	1.51×10^{40}	1.743	0.563	1.033	1.785	1.529	2.173	1.033	1.785
E15	1.60	0.80	2.84×10^{-9}	6.50×10^{4}	1.50×10^{40}	1.760	0.640	1.106	1.852	1.597	2.229	1.106	1.852
E16	1.60	0.85	2.67×10^{-9}	6.39×10^{4}	1.48×10^{40}	1.777	0.723	1.185	1.926	1.670	2.291	1.185	1.926
E17	3.20	0.70	3.24×10^{-9}	8.22×10^{4}	3.36×10^{40}	3.118	0.490	1.013	2.685	2.429	3.228	1.013	2.685
E18	3.20	0.75	3.03×10^{-9}	8.06×10^{4}	3.32×10^{40}	3.149	0.563	1.080	2.735	2.479	3.263	1.080	2.735
E19	3.20	0.80	2.84×10^{-9}	7.91×10^{4}	3.29×10^{40}	3.177	0.640	1.152	2.792	2.536	3.306	1.152	2.792
E20	3.20	0.85	2.67×10^{-9}	7.77×10^{4}	3.26×10^{40}	3.205	0.723	1.231	2.856	2.600	3.357	1.231	2.856

Table 1. Some representative physical parameters of the ejecta models are summarized in this table. The first column is the model name. The parameters of group 1 models span from column 2 to column 10, they are the radiation to gas energy ratio, ratio of ejecta speed to escape speed, gas density, temperature, radiation energy luminosity at $r_{\rm in}$, the ratio between the isotropic radiation pressure $p_{\rm rad} = \mathcal{E}/3$ and gas pressure, and three escape ability parameters ζ_1, ζ_2, and ζ_3, as defined in Equation 20 and 22. From columns 11 to 14, they correspond to the ζ_3 of groups 2 to 5. Each group has models from E1 to E20, but all groups have the same corresponding values of $\bar{v}_{\rm ej}$, $\rho_{\rm ej}$, and $T_{\rm g}$.

advection and transport [1]. Thus, the momentum and radiation transport equations we solve for this group reduce to

$$\frac{\partial E}{\partial t} + \nabla\cdot[(E+p)\mathbf{v}] = G^0 - \rho\mathbf{v}\cdot\nabla\phi, \quad (18)$$

$$\frac{\partial \mathcal{E}}{\partial t} + \nabla\cdot(\mathbf{F}_r + \mathcal{E}\mathbf{v}) = -G^0. \quad (19)$$

This radiation transport model (excluding the radiation advection term) is usually used in astrophysical problems when the radiation pressure is unimportant (Bhandare et al. 2024). Given that this group has the same ejecta's temperature, density, and velocity, it has the same amount of total energy as group 1.

We define and calculate ζ_1, ζ_2, and ζ_3 to approximately gauge the ability of the ejecta to escape the gravity of the central object,

$$\zeta_1 = \frac{\Delta e_k r_{\rm in}}{GM_\star \Delta M_{\rm ej}}, \quad (20)$$

$$\zeta_2 = \frac{(\Delta e_{\rm g} + \Delta e_k) r_{\rm in}}{GM_\star \Delta M_{\rm ej}}, \quad (21)$$

$$\zeta_3 = \frac{(\Delta\mathcal{E} + \Delta e_{\rm g} + \Delta e_k) r_{\rm in}}{GM_\star \Delta M_{\rm ej}}, \quad (22)$$

where $\Delta e_k, \Delta e_g$, and $\Delta\mathcal{E}$ are the kinetic, internal and radiation energy in the ejecta, calculated by,

$$\Delta e_k = \dot{e}_k \Delta t = \frac{\dot{M} v_{\rm ej}^2 \Delta t}{2}, \quad (23)$$

$$\Delta e_g = \dot{e}_g \Delta t = \frac{\dot{M} e_{\rm g} \Delta t}{\rho}, \quad (24)$$

$$\Delta\mathcal{E} = \dot{\mathcal{E}}_r \Delta t = \frac{\dot{M}\mathcal{E}\Delta t}{\rho}. \quad (25)$$

Typically, ζ_1 serves as a conservative estimate of the gas's ability to escape the system. Some literature sug-

[1] In fact, one can also calculate the $\mathcal{P}_r$ of this group according to Equation 8. But its effect is not taken into account.

gests that the recombination energy may not be efficient in unbinding the envelope (Grichener et al. 2018; Soker et al. 2018) (in the absence of radiation transport), which means that ζ_2 is not effective in measuring the gas's ability to escape. But we may need to reevaluate the impact of EoS after incorporating radiation transport and radiation pressure. Meanwhile, Chen & Ivanova (2024) found that $a_{\rm rad}$ may exceed g when the ejecta is ionized. Thus, we incorporate both $\mathcal{E}$ and $e_{\rm g}$ in ζ_3 as an optimistic measure of the gas's ability to escape. The potential synergy between the radiation pressure and recombination processes may realize their power to unbind the envelope.

3. SIMULATION RESULTS

We evolve all the simulations for 500 days, as most dynamical phenomena have faded at this time.

3.1. *A typical evolution of the ejecta*

The overall ejecta evolution are similar between different models, we present the evolution of model E10 in Figure 1 as an example. Panel 0 shows the evolution of density and the contour of $v_r = 0$. The $v_r = 0$ contour divides the ejecta into the outgoing and fallback parts. The fallback material can pass through the inner boundary and will no longer influence the evolution of the ejecta. Panel 1 shows the radiation luminosity through a spherical shell, calculated by $L_{37} = 4\pi r^2 F_r/(10^{37}{\rm erg}\cdot{\rm s}^{-1})$, where $F_r = \mathbf{F}_r \cdot \hat{r}$ is radius and time dependent. Consider the plots in panel 4 and panel 5, which show the temperature and mean atomic weight μ, we can conclude that the luminosity increases as the ejecta expands, but rapidly decreases when all the hydrogen recombines. Similarly, the opacity, shown in panel 2, maintains a high level when the hydrogen is ionized, because of the free-free scattering, decreases more than 100 times when the hydrogen recombines. Therefore, from panel 1 and panel 2, we can conclude that the radius where the majority of the radiation flux emerges, overlaps with the recombination front. As a result, the variable $a_{\rm rad}/g$, shown in panel 3, reaches a maximum right below the recombination front, because it is a kind of radiative-driven outflow, whose strength is determined by the product of radiation flux and opacity. When $a_{\rm rad}/g > 1$, the radiation pressure can effectively accelerate the ejecta. The gas pressure gradient may also accelerate the ejecta, shown in panel 7, with the same colormap and scale as panel 3. The gas pressure gradient is relatively more important in gas energy dominated ejecta, e.g. $\mathcal{E}/e_{\rm g} \ll 1$. We define

$$\xi = \frac{v^2 r}{2GM_\star} \tag{26}$$

and plot the variable in panel 6. It is a conservative measure of the gas's ability to escape. Overall, the radiation and gas pressure gradients help some gas to escape the system.

3.2. *Physical processes to unbind the envelope*

In Section 3.1, we have seen that both the radiation and gas pressure gradients could promote the unbinding the the envelope. We shall further analyze their relative importance on the envelope unbinding with various simulations.

3.2.1. *Radiation transport and radiation pressure*

The importance of the radiation pressure in unbinding the ejecta can be further demonstrated by comparing the simulations from the baseline, pure hydrodynamic, and no radiation pressure effect groups (groups 1, 4, and 5). We sum up the gas mass that satisfies $\xi > 1$ at the end of our simulation ($t = 500$day) to obtain $M_{\rm esc}$, define

$$\eta = M_{\rm esc}/\Delta M_{\rm ej} \tag{27}$$

as the mass unbound fraction, and plot their results in Figure 2. The dots on the solid, dashed, and dotted lines are the results from groups 1, 4, and 5, respectively. The baseline group with radiation pressure usually has the highest η among the three groups (except for model E1, discussed later), because it has radiation energy and radiation pressure that help to accelerate the ejecta while the other two groups can only accelerate the ejecta through the gas pressure gradient. In particular, the baseline group and no radiation pressure effect group differ only in the presence/absence of radiation pressure, while all of their other physical conditions are the same, providing a strong evidence that $\mathcal{P}_r$ is important in accelerating the ejecta. On the other hand, The pure hydrodynamic group has a higher η than the no radiation pressure effect group when $\mathcal{E}/e_{\rm g} < 1$ and a comparatively lower η when $\mathcal{E}/e_{\rm g} > 1$. The reversed trend reflects some RHD processes. We give a qualitative explanation as follows. The pure hydrodynamic group only has gas energy, while the no radiation pressure effect group has some extra radiation energy, but radiation transport continuously removes energy from the ejecta in the form of luminosity. Whether group 5 can accelerate more gas to escape velocity than group 4 may depend on two competing processes, the radiation energy luminosity $\dot{\mathcal{E}} = 4\pi r_{\rm in}^2 \mathcal{E} v_r$ (listed in Table 1) at the inner boundary and the luminosity $L = 4\pi r_{\rm out}^2 F_r(r_{\rm out})$ (Figure 6 has some representative light curves) at the outer boundary. There are two scenarios:

- If $\dot{\mathcal{E}} \gg L$, which is more likely when $\mathcal{E}$ is large, the gas may be heated by the radiation flux from the

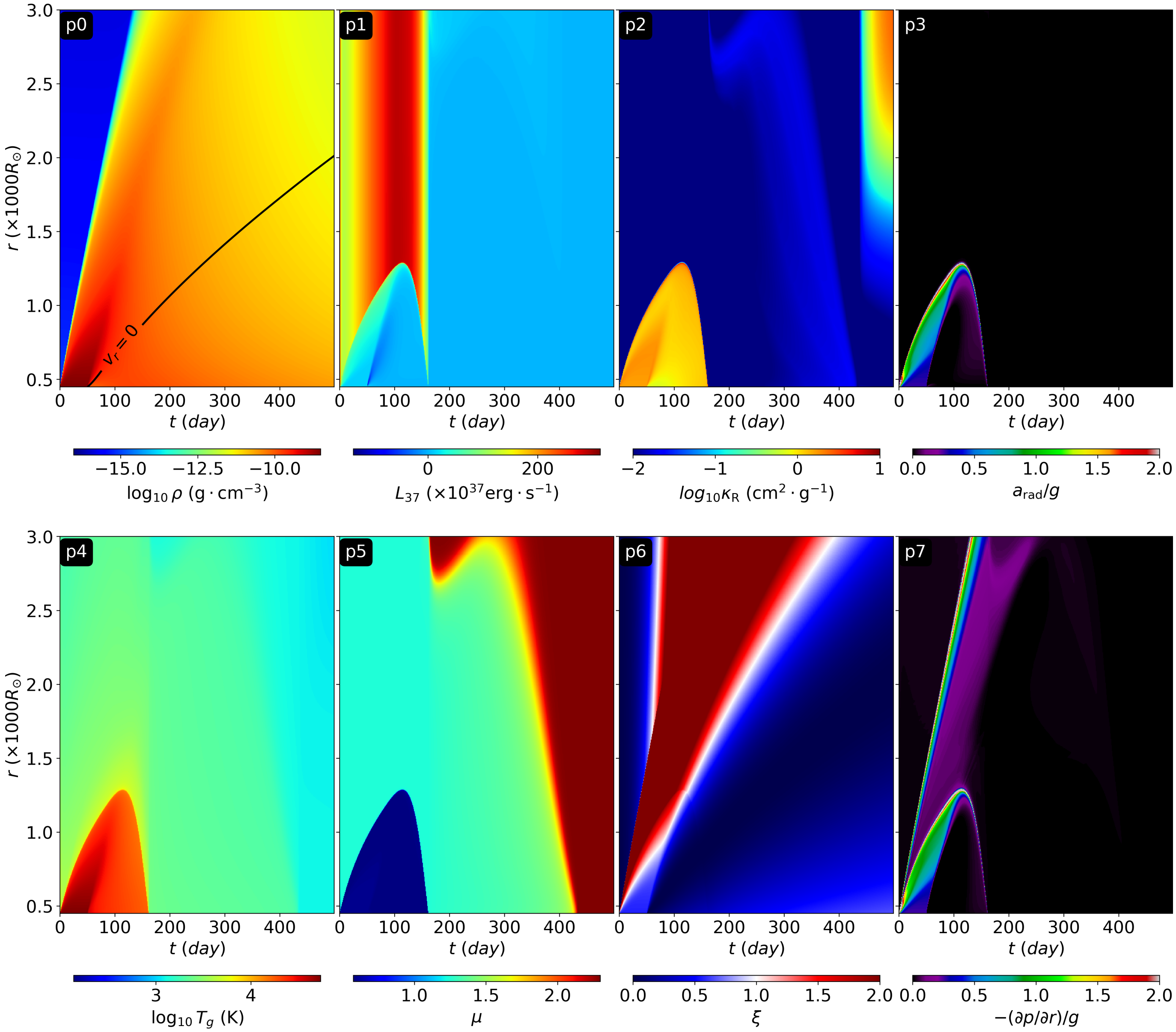

Figure 1. The evolution of model E10 ($\mathcal{E}/e_g = 0.8, \bar{v}_{ej} = 0.75$) from the baseline group. In each panel, the x-axis is time in days, and the y-axis is the r coordinate in $1000R_\odot$. From panel 0 to 7, they are the evolution of the density in g·cm^{-3}, luminosity in 10^{37}erg · s^{-1}, Rosseland mean opacity in cm^2·g^{-1}, radiation pressure acceleration compared to the gravitational force, gas temperature in K, mean atomic weight, conservative escape measure defined Equation 26, and negative pressure gradient compared to the gravitational force.

inner boundary, and maintain a steeper gas pressure gradient than the pure hydrodynamic group simulations.

- If $\dot{\mathcal{E}} \lesssim L$, which is more likely when $\mathcal{E}$ is small, the radiation flux from the inner boundary may not effectively heat the gas because of the fast energy loss. Moreover, $\dot{\mathcal{E}}$ is present only during the ejection phase, but the luminosity is persistent, therefore, the overall gas pressure gradient may be flatter than that in the pure hydrodynamic group simulations.

Since $L \propto r^2$, we anticipate that $\mathcal{E}$ could play a more important role in accelerating the ejecta in CEE with small sizes. The above-mentioned competing physical processes could also be the reason that the η of the pure hydrodynamic group is slightly larger than the baseline group in E1 model.

To demonstrate the correlation between $\mathcal{E}/e_g$ and a_{rad}, we plot the evolution of a_{rad} during the first 200

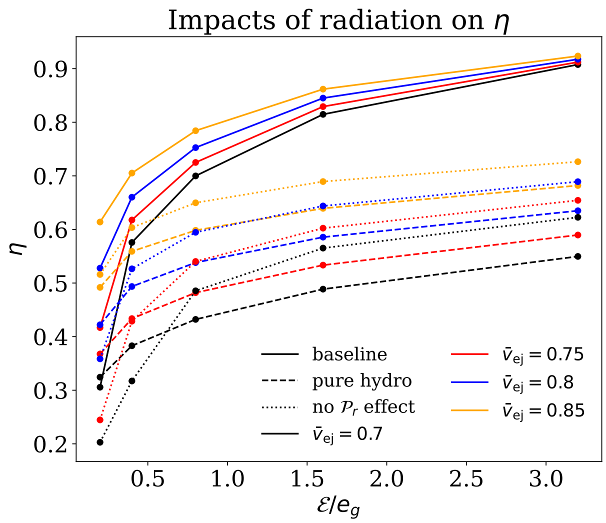

Figure 2. The unbound mass fraction η with different $\mathcal{E}/e_g$ and $\bar{v}_{ej}$. The baseline, pure hydrodynamic and no radiation pressure effect group are results from groups 1, 4 and 5.

days of models E2, E6, E10, E14, and E18, which have $\bar{v}_{ej} = 0.75$ and $\mathcal{E}/e_g \in \{0.2, 0.4, 0.8, 1.6, 3.2\}$ in Figure 3. As $\mathcal{E}/e_g$ increases, a_{rad} increases significantly. Consequently, η increases as $\mathcal{E}/e_g$ increases, shown by the solid black line in Figure 2.

3.2.2. *Realisitic EoS v.s. γ-law gas*

We compare the simulations from groups 1, 2, and 3 to demonstrate the impact of different EoS on envelope unbinding. Figure 4 shows η of the corresponding EoS at the end of the simulation. At low $\mathcal{E}/e_g$, the difference of η in the three EoS is more significant because their envelopes are gas energy/pressure dominated, and the EoS of gas should play a more important role. When the envelope becomes radiation energy dominated, all EoSs give relatively similar results because their envelopes are all radiation-like. In Table 1, $\zeta_{3,G2} < \zeta_{3,G1} < \zeta_{3,G3}$ for all models. As expected, group 2, the $\gamma_1 = 1.4$ simulations have the lowest M_{esc}. Overall, the baseline group has higher η than the $\gamma_2 = 1.1$ group simulations, despite that $\zeta_{3,G3} > \zeta_{3,G1}$. We attempt to analyze this counterintuitive phenomenon by taking model E1 as an example. We plot out the sum and different components of pressure gradients on the ejecta in Figure 5. The first row shows the combined acceleration effect from the radiation and gas pressure gradients with the realistic EoS, $\gamma_1 = 1.4$, and $\gamma_2 = 1.1$ simulations, respectively. Overall, the acceleration of $\gamma_1 = 1.4$ is smaller compared to the other two, possibly because of its lower $\zeta_{3,G2}$. The realistic EoS model has a slightly higher acceleration during the early time and in the small radius region compared to the $\gamma_2 = 1.1$ model, because its pressure gradient is higher, shown in the second row of Figure 5. The acceleration at small radii is more important because $g \propto 1/r^2$. Therefore, EoS is important in the acceleration and unbinding processes of the envelope.

We can further break down the gas pressure gradient of the realistic EoS simulation into three components,

$$
\begin{aligned}
-\frac{\partial p}{\partial r} &= -\frac{p}{\rho}\frac{\partial \rho}{\partial r} - \frac{p}{T}\frac{\partial T}{\partial r} + \frac{p}{\mu}\frac{\partial \mu}{\partial r}, \\
&= -\nabla_\rho p - \nabla_T p - \nabla_\mu p. \qquad (28)
\end{aligned}
$$

We plot each component in the third row of Figure 5. It turns out that $\nabla_\rho p$ is the major source of the pressure gradient, and $\nabla_\mu p$ is negligible compared to the other two.

3.3. *Impacts on the light curves*

We have seen and discussed how $\mathcal{E}/e_g$, EoS, and $\bar{v}_{ej}$ can affect envelope unbinding. Meanwhile, they could also affect the light curve of the ejecta. To investigate this part, we define the light curve as the luminosity calculated at the outer boundary,

$$L = 4\pi r_{out}^2 F_r(r_{out}), \qquad (29)$$

and present the results in Figure 6.

The top panel of Figure 6 shows the light curves of models with the same $\mathcal{E}/e_g = 0.2$ but $\bar{v}_{ej} \in \{0.7, 0.75, 0.8, 0.85\}$ from the baseline group. Because the ejecta with high $\bar{v}_{ej}$ expands faster than the low $\bar{v}_{ej}$, it also becomes optically thin more quickly, reaches peak luminosity, and fades out earlier. Overall, the four light curves are similar, indicating that $\bar{v}_{ej}$ may not be a decisive parameter in the shape of the light curves, but further parameter study is warranted. The middle panel shows the light curves from models with the same $\bar{v}_{ej} = 0.75$ but $\mathcal{E}/e_g \in \{0.2, 0.4, 0.8, 1.6, 3.2\}$ from the baseline group. The five light curves are drastically different, showing a trend that high $\mathcal{E}/e_g$ ejecta has high luminosity but dims earlier, because the radiation pressure in the high $\mathcal{E}/e_g$ ejecta accelerates the ejecta more efficiently, and the ejecta become larger and tenuous more quickly, leading to the phenomenon in the middle panel. Meanwhile, the source term $-\mathcal{P}_r : \nabla \mathbf{v}$ has a direct impact on the energy Equation 4, consumes more radiation energy in the case of acceleration. The bottom panel shows light curves of model E2 from group 1, 2, and 3. The three light curves are also drastically different, with $\gamma_2 = 1.1$ being the most luminous one, because it has more energy in the ejecta ($\zeta_{3,G3} > \zeta_3 > \zeta_{3,G2}$ and they have the same amount of kinetic energy). However, its luminosity decreasing rate is larger than the one with realistic EoS from the baseline group between 200 and

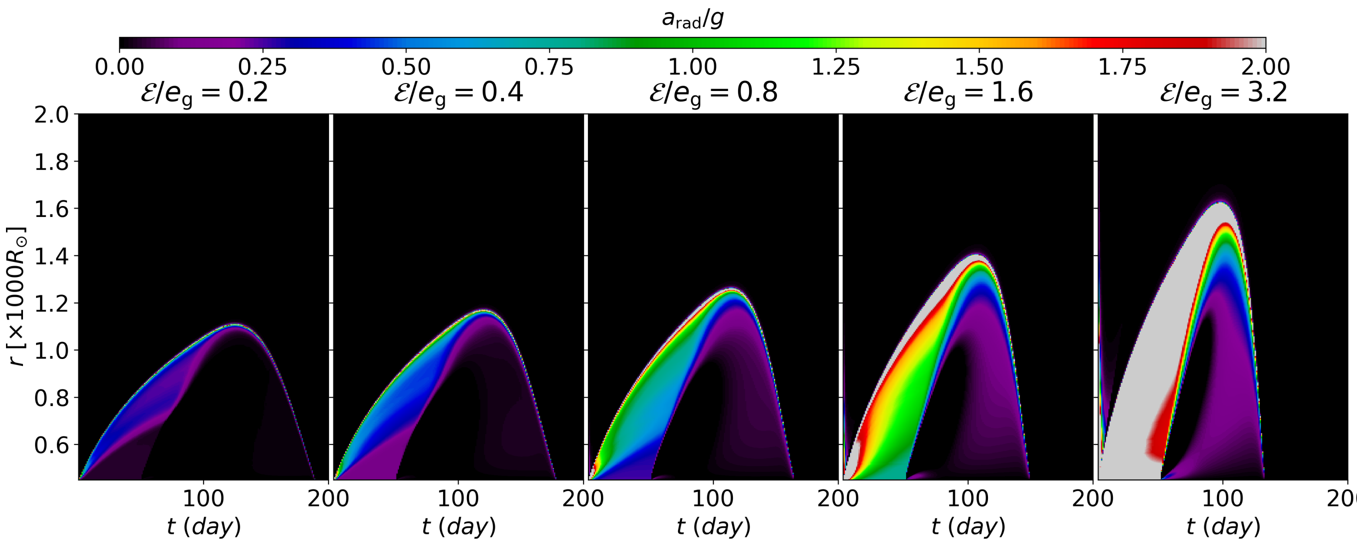

Figure 3. The evolution of $a_{\rm rad}$ of models E2, E6, E10, E14, and E18 from the baseline group. They all have $\bar{v}_{\rm ej} = 0.75$, but their $\mathcal{E}/e_{\rm g} \in \{0.2, 0.4, 0.8, 1.6, 3.2\}$, respectively. The grey and red color region indicates our newly discovered radiation pressure dominated layer below the recombination front.

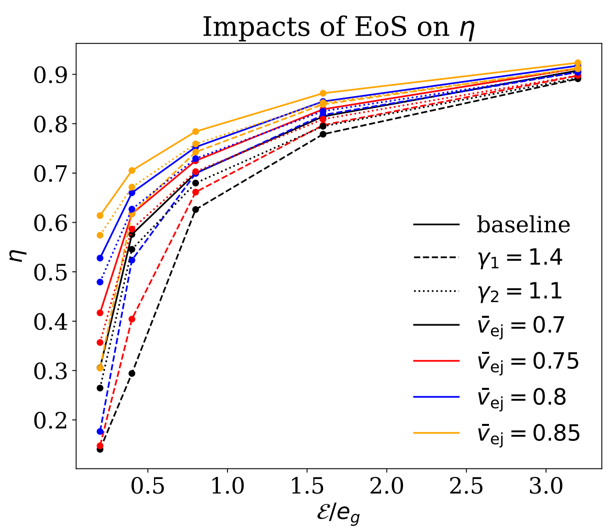

Figure 4. The fraction of the unbound mass η v.s. different $\mathcal{E}/e_{\rm g}$, $\bar{v}_{\rm ej}$, and EoSs. The baseline, $\gamma_1 = 1.4$, and $\gamma_2 = 1.1$ are results from groups 1, 2, and 3.

450 days, because the recombination process from H to H_2 is providing the energy to the ejecta in the simulation with realistic EoS. To demonstrate, we plot the total mass fraction of H_2 within the hydrogen species,

$$\bar{\chi}_{\rm H_2} = M_{\rm H_2}/(XM) \tag{30}$$

where $M_{\rm H_2}$ and M are the total mass of H_2 and total mass in the computational domain, respectively. The time of the reduced luminosity decay rate of the baseline group simulation overlaps with the rise of $\bar{\chi}_{\rm H_2}$. In reality, the recombination of H is usually associated with dust formation, the release of this binding energy may power the infrared band and make the diffused ejecta resemble the unusual infrared transients observed by the Spitzer telescope (Kasliwal et al. 2017), if the ejecta is massive enough.

4. CONCLUSIONS AND DISCUSSIONS

We investigate the ejecta acceleration and envelope unbinding processes that could be associated with the plunge-in phase of CEE using a 1D RHD model. We perform a parameter survey to assess the influence of $\mathcal{E}/e_{\rm g}$, $\bar{v}_{\rm ej}$, EoS (realistic or γ-law gas), and the inclusion of radiation pressure on the system's dynamics and light curves. From this analysis, we draw four main conclusions.

1. Qualitatively, radiation pressure is the most direct and effective way to accelerate the envelope to escape velocity, which can be seen by comparing the simulations from group 1 and group 5 in Section 3.2.1.

2. Quantitatively, a high value of $\mathcal{E}/e_{\rm g}$ can give rise to significant radiation pressure acceleration (Figure 3), especially in a layer below the recombination front where the luminosity is high because of low optical depth and the opacity is also high due to free-free and bound-free scattering. It can also lead to a large mass unbound fraction η (Section 3.2.1), and a higher peak in the light curve (Section 3.3).

3. The gas pressure gradient also contributes to the acceleration of the ejecta, with decreasing importance compared to the radiation pressure when

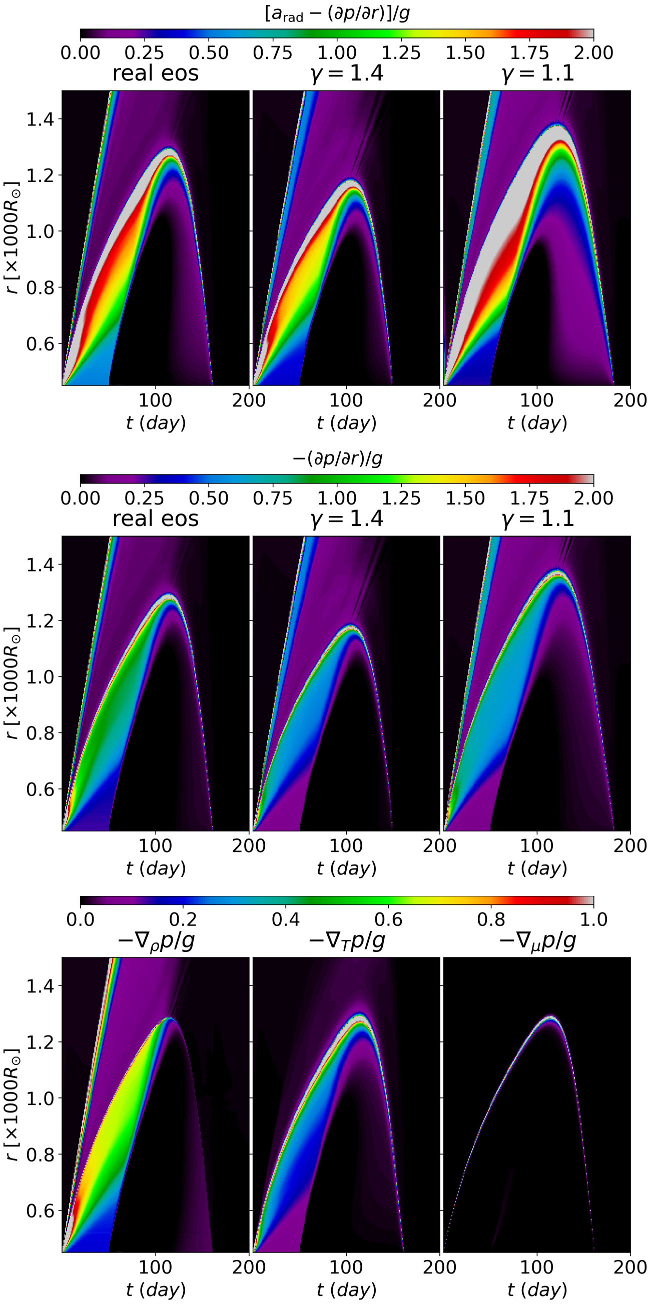

Figure 5. First row: the combined acceleration rate $[a_{\rm rad} - \frac{\partial p}{\partial r}]/g$ of the model E2 from groups 1, 2, and 3. Second row: $-(\frac{\partial p}{\partial r})/g$ of the model E2 from groups 1, 2, and 3. Third row: the break down of $-(\frac{\partial p}{\partial r})/g$ of model E2 into $-\nabla_\rho p/g$, $-\nabla_T p/g$, $-\nabla_\mu p/g$, defined in Equation 28. To enhance the contrast, the colormap range of the first row is $[0, 2]$, different from the other two.

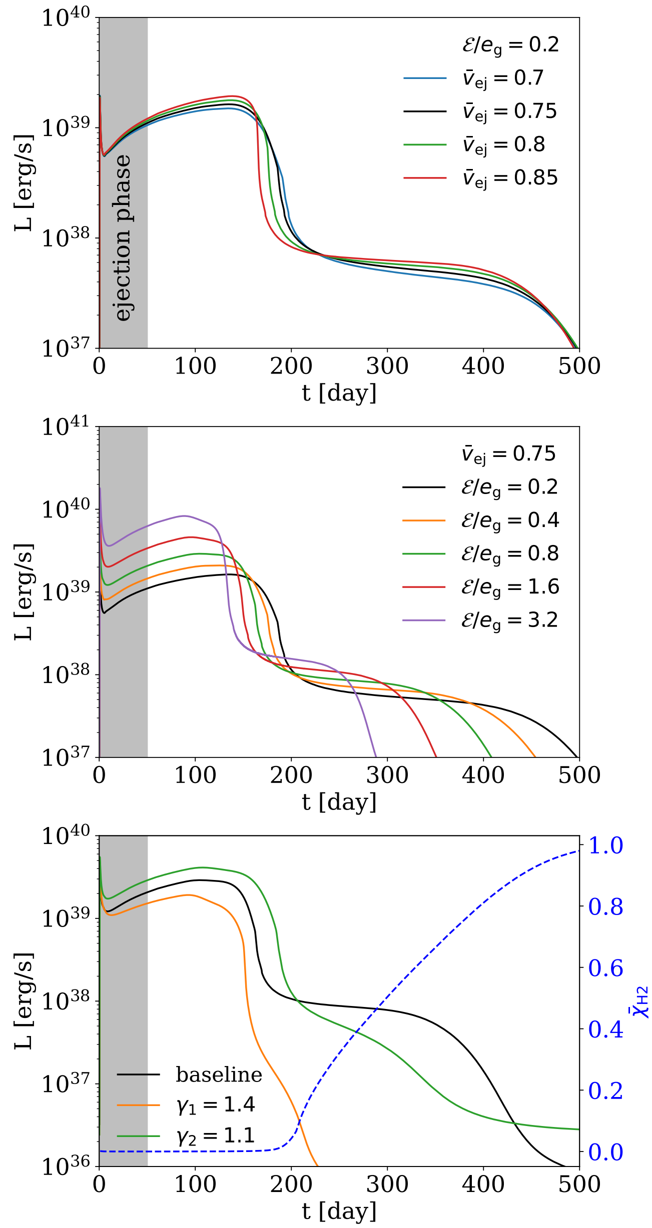

Figure 6. The grey color shaded regions highlight the ejection phase (the first 50 days). Top panel: light curves of model E1, E2, E3, and E4 ($\mathcal{E}/e_{\rm g} = 0.2$ but $\bar{v}_{\rm ej} \in \{0.7, 0.75, 0.8, 0.85\}$) of the baseline group. Middle panel: light curves of model E2, E6, E10, E14, and E18 (same $\bar{v}_{\rm ej} = 0.75$ but $\mathcal{E}/e_{\rm g} \in \{0.2, 0.4, 0.8, 1.6, 3.2\}$) of the baseline group. Bottom panel: light curves of model E2 from the realistic EoS, $\gamma_1 = 1.4$, and $\gamma_2 = 1.1$ group. The black lines in each panel are the same model, e.g., model E2 of group 1. The secondary y-axis shows the total mass fraction of H_2.

$\mathcal{E}/e_{\rm g}$ increases. The gas pressure gradient in the realistic EoS gas is slightly steeper than the γ-law gas (Section 3.2.2), making the envelope easier to become unbound.

4. The recombination process from H to H_2 provides latent heat to the ejecta in the late time evolution, creating a plateau in the light curve (Figure 6).

In reality, the envelope unbinding process is much more complicated, which involves a burst of energy deposition deep inside an envelope, and convective motion that dissipates the extra energy. The current model is limited to the dynamical phase of supersonic envelope ejection due to the absence of more a realistic inner boundary condition. A realistic inner boundary, connected to the inspiral of the binary cores, is required to provide the gas and radiation pressure at the inner boundary, as well as the radiation and convective luminosities, that drive the continuous unbinding of the envelope. Developing such a boundary presents an opportunity for future work.

Moreover, as a 1D model, it has difficulty in incorporating the angular momentum and asymmetry self-consistently, but it is well known that CEE involves a considerable amount of angular momentum transfer. The impact of angular momentum and asymmetric outflow on the envelope unbinding process and light curves may be answered by 2D/3D models with parameter surveys.

The author thanks the anonymous reviewer whose suggestions have greatly improved the quality of this paper. The author also thanks Xue-Ning Bai (白雪宁), Yuran Chen (陈雨然), and Jingze Ma (马竟泽) for constructive discussions. This work is financially supported by the National Science Foundation of China under grants No. 12103028, 12342501, 12473030, Tsinghua University Dushi Program at Tsinghua University. The Center of High Performance Computing at Tsinghua University provided the computational resources. Z.C. thanks the International Centre of Supernovae (ICESUN), Yunnan Key Laboratory of Supernova Research for providing a vibrant environment for discussion.

Software: `Guangqi` (Chen & Bai submitted), `Matplotlib` (Hunter 2007), `Petsc` (Balay et al. 1997, 2024)

APPENDIX

A. ENERGY CONSERVATION

Because the gravitational and radiation pressure are treated as explicit source terms in the energy equation, and the implicit radiation transport solver also cannot conserve energy to machine precision, it is necessary to examine the energy conservation in our simulations. Dimensional analysis shows that (Colombo et al. 2019),

$$\nabla\cdot\mathcal{P}_r \approx -\frac{\rho\kappa_{\rm R}\mathbf{F}_r}{c}, \tag{A1}$$

when $v_{\rm gas}/c \ll 1$. Because this condition is satisfied in all of our simulations, we analyze the energy conservation of our simulations by substituting Equation A1 into 3, and obtain

$$\frac{\partial E}{\partial t} + \nabla\cdot[(E+p)\mathbf{v}] = -\rho\mathbf{v}\cdot(\nabla\cdot\mathcal{P}_r + \nabla\phi) + G^0. \tag{A2}$$

Adding Equation A2 and 4, we obtain,

$$\frac{\partial(E+\mathcal{E}+\rho\phi)}{\partial t} + \nabla\cdot[(E+p+\mathcal{E}+\mathcal{P}_r+\rho\phi)\cdot\mathbf{v}+\mathbf{F}_r] = 0, \tag{A3}$$

where we have used $\nabla\cdot(\rho\mathbf{v}\phi) = \rho\mathbf{v}\cdot\nabla\phi + \phi\nabla\cdot(\rho\mathbf{v})$ and the mass conservation equation.

We examine the energy conservation by calculating the energy balance at the end of the simulations. The error of the energy $E_{\rm err}$ is calculated by,

$$E_{\rm err} = ET_{\rm final} - ET_{\rm init} + \int[F(r_{\rm in}) - F(r_{\rm out})]dt \tag{A4}$$

$$ET = \int_V (E+\mathcal{E}+\rho\phi)dV \tag{A5}$$

$$F(r) = \int_S [(E+p+\rho\phi+\mathcal{E}+\mathcal{P}_r)\cdot\mathbf{v}+\mathbf{F}_r]\cdot\mathbf{dS} \tag{A6}$$

where ET is the total energy in the computational domain, and $F(r)$ is the area integrated energy flux at radius r. Because $ET_{\rm init}$ is 5 orders of magnitude smaller than $ET_{\rm final}$, it is negligible. At the inner boundary, $\mathbf{F}_r(r_{\rm in}) = 0$ is determined by the boundary condition, and the environment at $r_{\rm in}$ is always optically thick, thus, $\mathcal{P}_r\cdot\mathbf{v} \approx \mathcal{E}\mathbf{v}/3$. Combining the radiation pressure term with the radiation advection term, we get $4\mathcal{E}\mathbf{v}/3 = 4\mathcal{E}v_{r_{\rm in}}\hat{r}/3$, where $v_{r_{\rm in}}$ denotes the velocity at $r = r_{\rm in}$. At the outer boundary, the environment is always set to optically thin, thus, $|\mathcal{P}_r\cdot\mathbf{v}| \approx |\mathcal{E}v_{r_{\rm out}}| \ll \mathcal{E}c \approx F_r$ is negligible compared to the radiation transport. We further define several more energies and two relative errors by,

$$\Delta_N E_{\rm hyd} = 4\pi r_{\rm in}^2 \int_0^{N{\rm day}} [(E+p)v_{r_{\rm in}}]dt \tag{A7}$$

$$\Delta_N E_{\rm rad} = 4\pi r_{\rm in}^2 \int_0^{N{\rm day}} \frac{4\mathcal{E}v_{r_{\rm in}}}{3}dt \tag{A8}$$

$$\Delta_N E_{\rm rhd} = \Delta_N E_{\rm hyd} + \Delta_N E_{\rm rad} \tag{A9}$$

$$\Delta_N E_{\rm gra} = 4\pi r_{\rm in}^2 \int_0^{N{\rm day}} \rho\phi v_{r_{\rm in}}dt \tag{A10}$$

$$\Delta_N E_{r_{\rm in}} = \Delta_N E_{\rm hyd} + \Delta_N E_{\rm rad} + \Delta_N E_{\rm gra} \tag{A11}$$

$$\delta E_{\rm err,1} = \frac{E_{\rm err}}{\Delta_{50}E_{r_{\rm in}}}, \tag{A12}$$

$$\delta E_{\rm err,2} = \frac{E_{\rm err}}{\Delta_{50}E_{\rm hydro} + \Delta_{50}E_{\rm rad}}. \tag{A13}$$

In particular, $\delta E_{\rm err,1}$ measures the relative error between $E_{\rm err}$ and the total incoming energy during the ejection phase.

It can be calculated that $\Delta_{50}E_{\rm gra} = -8.67 \times 10^{46}$erg. Because ϕ is negative, $\Delta_N E(r_{\rm in})$ could be quite close to 0, we define $\delta E_{\rm err,2}$ as a secondary measure of the relative energy error. We list the relevant energy fluxes and relative errors in Table 2. Clearly, $\delta E_{\rm err,2} \leq 1.4\%$ in our 20 simulations, indicating very good energy conservation. The biggest $\delta E_{\rm err,2}$ happens to the simulations with the biggest $\mathcal{E}/e_{\rm g}$. When $\mathcal{E}/e_{\rm g} \leq 1.6$, which could be enough for the many binary cases, $\delta E_{\rm err,2} \leq 0.33\%$. However, $\delta E_{\rm err,1}$ may not be as small as $\delta E_{\rm err,2}$ if $\Delta_{50}E_{\rm rhd}$ and $\Delta_{50}E_{\rm gra}$ cancels out.

Finally, we note that the total injected energy $\Delta_{50}E_{\rm rhd}$ is in the range of $[10^{47}, 3\times10^{47}]$ erg, which is much smaller than the gravitational energy released ($\sim 10^{48}$ erg) by a typical massive binary during the plunge-in phases (Fragos et al. 2019). Thus, a full CEE of these kind of binary may involve more mass ejection and brighter light curve.

B. NUMERICAL CONVERGENCE

The RHD system with complex EoS is highly nonlinear and multiscale. To obtain the converged solutions, we use relatively small sub-timesteps when we solve the radiation transport equation, with $n_{\rm sub} = 6$ and $q_t = 1.4$. To examine whether a solution is truly converged, we use L in Equation 29 to test the convergence, because it is very sensitive to the change of any parameters in our model. We take model E1 as an example and double the base resolution to $N_x = 3072$. The doubled base resolution will lead to roughly halved hydrodynamic and radiation time-steps. The luminosities from the two simulations and their relative difference are presented in Figure 7. The small relative difference

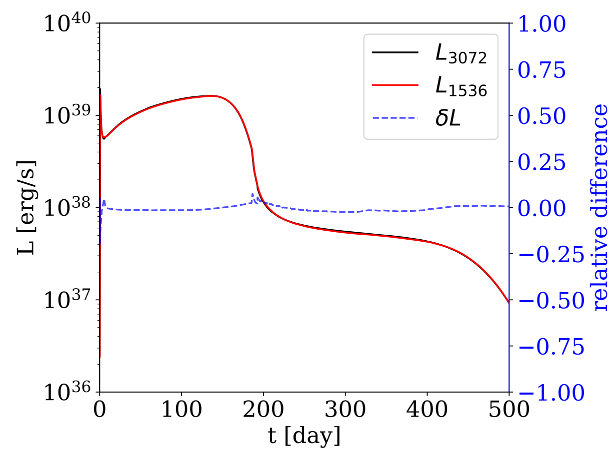

Figure 7. The luminosity L (Equation 29) of model E2. The black and red lines are the results of model E1 with $N_x = 3072$ and $N_x = 1536$ base resolution, respectively. The blue dashed line is their relative difference, $\delta L = (L_{3072} - L_{1536})/L_{3072}$.

indicates that our simulations are close to converged solutions. Other models have qualitatively similar results.

REFERENCES

Balay, S., Gropp, W. D., McInnes, L. C., & Smith, B. F. 1997, in Modern Software Tools in Scientific Computing, ed. E. Arge, A. M. Bruaset, & H. P. Langtangen (Birkhäuser Press), 163–202

Balay, S., Abhyankar, S., Adams, M. F., et al. 2024, PETSc/TAO Users Manual, Tech. Rep. ANL-21/39 - Revision 3.22, Argonne National Laboratory, doi: 10.2172/2205494

Bhandare, A., Commerçon, B., Laibe, G., et al. 2024, A&A, 687, A158, doi: 10.1051/0004-6361/202449594

Blagorodnova, N., Kotak, R., Polshaw, J., et al. 2017, ApJ, 834, 107, doi: 10.3847/1538-4357/834/2/107

Blagorodnova, N., Klencki, J., Pejcha, O., et al. 2021, A&A, 653, A134, doi: 10.1051/0004-6361/202140525

Cai, Y. Z., Pastorello, A., Fraser, M., et al. 2019, A&A, 632, L6, doi: 10.1051/0004-6361/201936749

Chamandy, L., Carroll-Nellenback, J., Blackman, E. G., et al. 2024, MNRAS, 528, 234, doi: 10.1093/mnras/stae036

Chamandy, L., Frank, A., Blackman, E. G., et al. 2018, MNRAS, 480, 1898, doi: 10.1093/mnras/sty1950

Chen, X., Liu, Z., & Han, Z. 2024, Progress in Particle and Nuclear Physics, 134, 104083, doi: 10.1016/j.ppnp.2023.104083

model Ejecta (1)	$ET_{\rm final}$ (erg) (2)	$\Delta_{50}E_{\rm hyd}$ (erg) (3)	$\Delta_{50}E_{\rm rad}$ (erg) (4)	$\Delta_{50}E_{\rm rhd}$ (erg) (5)	$\Delta_{50}E_{r_{\rm in}}$ (erg) (6)	$\int Ldt$ (erg) (7)	$E_{\rm err}$ (erg) (8)	$\delta E_{\rm err,1}$ % (9)	$\delta E_{\rm err,2}$ % (10)
E1	-3.32×10^{45}	8.11×10^{46}	8.44×10^{45}	8.95×10^{46}	2.83×10^{45}	1.98×10^{46}	1.76×10^{43}	0.62	0.020
E2	-1.52×10^{45}	8.67×10^{46}	8.31×10^{45}	9.50×10^{46}	8.34×10^{45}	2.10×10^{46}	4.06×10^{43}	0.49	0.043
E3	9.18×10^{44}	9.28×10^{46}	8.18×10^{45}	1.01×10^{47}	1.43×10^{46}	2.18×10^{46}	1.23×10^{44}	0.86	0.12
E4	4.24×10^{45}	9.93×10^{46}	8.04×10^{45}	1.07×10^{47}	2.06×10^{46}	2.21×10^{46}	2.07×10^{44}	1.0	0.19
E5	4.48×10^{45}	8.60×10^{46}	1.86×10^{46}	1.05×10^{47}	1.80×10^{46}	2.44×10^{46}	1.65×10^{44}	0.92	0.16
E6	7.33×10^{45}	9.19×10^{46}	1.85×10^{46}	1.10×10^{47}	2.37×10^{46}	2.55×10^{46}	1.70×10^{44}	0.72	0.15
E7	1.08×10^{46}	9.82×10^{46}	1.84×10^{46}	1.17×10^{47}	2.99×10^{46}	2.63×10^{46}	1.96×10^{44}	0.66	0.17
E8	1.50×10^{46}	1.05×10^{47}	1.83×10^{46}	1.23×10^{47}	3.65×10^{46}	2.68×10^{46}	2.18×10^{44}	0.60	0.18
E9	2.01×10^{46}	9.06×10^{46}	4.03×10^{46}	1.31×10^{47}	4.42×10^{46}	3.18×10^{46}	1.20×10^{44}	0.27	0.092
E10	2.36×10^{46}	9.64×10^{46}	4.00×10^{46}	1.36×10^{47}	4.97×10^{46}	3.26×10^{46}	1.46×10^{44}	0.29	0.11
E11	2.77×10^{46}	1.03×10^{47}	3.97×10^{46}	1.42×10^{47}	5.57×10^{46}	3.33×10^{46}	1.69×10^{44}	0.30	0.12
E12	3.25×10^{46}	1.09×10^{47}	3.94×10^{46}	1.49×10^{47}	6.21×10^{46}	3.39×10^{46}	1.88×10^{44}	0.30	0.13
E13	5.50×10^{46}	9.63×10^{46}	8.77×10^{46}	1.84×10^{47}	9.73×10^{46}	4.57×10^{46}	-6.03×10^{44}	−0.62	−0.33
E14	5.89×10^{46}	1.02×10^{47}	8.70×10^{46}	1.89×10^{47}	1.02×10^{47}	4.63×10^{46}	-5.03×10^{44}	−0.49	−0.27
E15	6.33×10^{46}	1.08×10^{47}	8.62×10^{46}	1.94×10^{47}	1.08×10^{47}	4.69×10^{46}	-4.52×10^{44}	−0.42	−0.23
E16	6.83×10^{46}	1.15×10^{47}	8.56×10^{46}	2.00×10^{47}	1.14×10^{47}	4.75×10^{46}	-3.82×10^{44}	−0.34	−0.19
E17	1.34×10^{47}	1.03×10^{47}	1.93×10^{47}	2.97×10^{47}	2.10×10^{47}	7.28×10^{46}	-4.21×10^{45}	−2.0	−1.4
E18	1.37×10^{47}	1.09×10^{47}	1.91×10^{47}	3.00×10^{47}	2.13×10^{47}	7.33×10^{46}	-3.47×10^{45}	−1.6	−1.2
E19	1.41×10^{47}	1.15×10^{47}	1.90×10^{47}	3.04×10^{47}	2.18×10^{47}	7.38×10^{46}	-2.96×10^{45}	−1.4	−0.97
E20	1.46×10^{47}	1.21×10^{47}	1.88×10^{47}	3.09×10^{47}	2.22×10^{47}	7.43×10^{46}	-2.56×10^{45}	−1.2	−0.83

Table 2. From column (2) to (6), the final total energy, $\Delta_{50}E_{\rm hyd}$, $\Delta_{50}E_{\rm rad}$, $\Delta_{50}E_{\rm rhd}$, and $\Delta_{50}E_{r_{\rm in}}$, defined from Equation A7-A11, column (7) is the total luminosity energy over the whole simulation, and the rest three columns are calculated by Equation A4, A12, and A13, respectively. The model with the largest $|\delta E_{\rm err,2}|$ is marked with the red color.

Chen, Z., & Bai, X. submitted, ApJS submitted

Chen, Z., Coleman, M. S. B., Blackman, E. G., & Frank, A. 2019, Journal of Computational Physics, 388, 490, doi: 10.1016/j.jcp.2019.03.016

Chen, Z., & Ivanova, N. 2024, ApJL, 963, L35, doi: 10.3847/2041-8213/ad2a47

Colombo, S., Ibgui, L., Orlando, S., et al. 2019, A&A, 631, A41, doi: 10.1051/0004-6361/201935991

Decin, L. 2021, ARA&A, 59, 337, doi: 10.1146/annurev-astro-090120-033712

Dominik, M., Belczynski, K., Fryer, C., et al. 2012, ApJ, 759, 52, doi: 10.1088/0004-637X/759/1/52

Fragos, T., Andrews, J. J., Ramirez-Ruiz, E., et al. 2019, ApJL, 883, L45, doi: 10.3847/2041-8213/ab40d1

Goldberg, J. A., Jiang, Y.-F., & Bildsten, L. 2022, ApJ, 929, 156, doi: 10.3847/1538-4357/ac5ab3

Gräfener, G., Owocki, S. P., Grassitelli, L., & Langer, N. 2017, A&A, 608, A34, doi: 10.1051/0004-6361/201731590

Grichener, A., Sabach, E., & Soker, N. 2018, MNRAS, 478, 1818, doi: 10.1093/mnras/sty1178

Han, Z.-W., Ge, H.-W., Chen, X.-F., & Chen, H.-L. 2020, Research in Astronomy and Astrophysics, 20, 161, doi: 10.1088/1674-4527/20/10/161

Hatfull, R. W. M., & Ivanova, N. 2025, ApJ, 982, 83, doi: 10.3847/1538-4357/ada6b8

Hatfull, R. W. M., Ivanova, N., & Lombardi, J. C. 2021, MNRAS, 507, 385, doi: 10.1093/mnras/stab2140

Hirai, R., & Mandel, I. 2022, ApJL, 937, L42, doi: 10.3847/2041-8213/ac9519

Höfner, S., & Olofsson, H. 2018, A&A Rv, 26, 1, doi: 10.1007/s00159-017-0106-5

Hunter, J. D. 2007, Computing in Science & Engineering, 9, 90, doi: 10.1109/MCSE.2007.55

Iaconi, R., Maeda, K., De Marco, O., Nozawa, T., & Reichardt, T. 2019, MNRAS, 489, 3334, doi: 10.1093/mnras/stz2312

Ivanova, N., & Nandez, J. L. A. 2016, MNRAS, 462, 362, doi: 10.1093/mnras/stw1676

Ivanova, N., Justham, S., Chen, X., et al. 2013, A&A Rv, 21, 59, doi: 10.1007/s00159-013-0059-2

Kalogera, V., & Webbink, R. F. 1998, ApJ, 493, 351, doi: 10.1086/305085

Kasliwal, M. M., Bally, J., Masci, F., et al. 2017, ApJ, 839, 88, doi: 10.3847/1538-4357/aa6978

Lau, M. Y. M., Hirai, R., González-Bolívar, M., et al. 2022a, MNRAS, 512, 5462, doi: 10.1093/mnras/stac049

Lau, M. Y. M., Hirai, R., Price, D. J., & Mandel, I. 2022b, MNRAS, 516, 4669, doi: 10.1093/mnras/stac2490

Lau, M. Y. M., Hirai, R., Price, D. J., Mandel, I., & Bate, M. R. 2025, A&A, 699, A274, doi: 10.1051/0004-6361/202554782

Levermore, C. D. 1984, JQSRT, 31, 149, doi: 10.1016/0022-4073(84)90112-2

Levermore, C. D., & Pomraning, G. C. 1981, ApJ, 248, 321, doi: 10.1086/159157

Liu, Z.-W., Röpke, F. K., & Han, Z. 2023, Research in Astronomy and Astrophysics, 23, 082001, doi: 10.1088/1674-4527/acd89e

Malygin, M. G., Kuiper, R., Klahr, H., Dullemond, C. P., & Henning, T. 2014, A&A, 568, A91, doi: 10.1051/0004-6361/201423768

Moreno, M. M., Schneider, F. R. N., Röpke, F. K., et al. 2022, A&A, 667, A72, doi: 10.1051/0004-6361/202142731

Nandez, J. L. A., & Ivanova, N. 2016, MNRAS, 460, 3992, doi: 10.1093/mnras/stw1266

Nandez, J. L. A., Ivanova, N., & Lombardi, Jr., J. C. 2014, ApJ, 786, 39, doi: 10.1088/0004-637X/786/1/39

Nandez, J. L. A., Ivanova, N., & Lombardi, J. C. J. 2015, MNRAS, 450, L39, doi: 10.1093/mnrasl/slv043

Ohlmann, S. T., Röpke, F. K., Pakmor, R., & Springel, V. 2016, ApJL, 816, L9, doi: 10.3847/2041-8205/816/1/L9

Ondratschek, P. A., Röpke, F. K., Schneider, F. R. N., et al. 2022, A&A, 660, L8, doi: 10.1051/0004-6361/202142478

Pastorello, A., Mason, E., Taubenberger, S., et al. 2019, A&A, 630, A75, doi: 10.1051/0004-6361/201935999

Pastorello, A., Fraser, M., Valerin, G., et al. 2021a, A&A, 646, A119, doi: 10.1051/0004-6361/202039952

Pastorello, A., Valerin, G., Fraser, M., et al. 2021b, A&A, 647, A93, doi: 10.1051/0004-6361/202039953

Prust, L. J., & Chang, P. 2019, MNRAS, 486, 5809, doi: 10.1093/mnras/stz1219

Ricker, P. M., & Taam, R. E. 2012, ApJ, 746, 74, doi: 10.1088/0004-637X/746/1/74

Sand, C., Ohlmann, S. T., Schneider, F. R. N., Pakmor, R., & Röpke, F. K. 2020, A&A, 644, A60, doi: 10.1051/0004-6361/202038992

Sander, A. A. C., & Vink, J. S. 2020, MNRAS, 499, 873, doi: 10.1093/mnras/staa2712

Semenov, D., Henning, T., Helling, C., Ilgner, M., & Sedlmayr, E. 2003, A&A, 410, 611, doi: 10.1051/0004-6361:20031279

Soker, N., Grichener, A., & Sabach, E. 2018, ApJL, 863, L14, doi: 10.3847/2041-8213/aad736

Tylenda, R., Hajduk, M., Kamiński, T., et al. 2011, A&A, 528, A114, doi: 10.1051/0004-6361/201016221

Vetter, M., Röpke, F. K., Schneider, F. R. N., et al. 2024, A&A, 691, A244, doi: 10.1051/0004-6361/202451579

Vetter, M., Roepke, F. K., Schneider, F. R. N., et al. 2025, arXiv e-prints, arXiv:2504.12213, doi: 10.48550/arXiv.2504.12213

Wilson, E. C., & Nordhaus, J. 2020, MNRAS, 497, 1895, doi: 10.1093/mnras/staa2088

—. 2022, MNRAS, 516, 2189, doi: 10.1093/mnras/stac2300

Xing, Z., Fragos, T., Zapartas, E., et al. 2025, A&A, 693, A27, doi: 10.1051/0004-6361/202451275